Honeycomb-like Mesoporous NiO−SnO$_2$/SO$_4^{2-}$ Solid Superacid for the Efficient Reaction of Methanol Oxidation

Yingying Gu[1,*], Pengyu Gao[1], Zhenzhen Yu[1], Yifen Hu[1], Zhen Xu[1], Chuan Zhang[1], Jing Li[2], Yarui An[1,**]

[1] College of Science, University of Shanghai for Science and Technology, Shanghai 200093, China
[2] Center of Public Experiment, University of Shanghai for Science and Technology, Shanghai 200093, China
[*]E-mail: yygu@usst.edu.cn, anyarui@usst.edu.cn

NiO−SnO$_2$/SO$_4^{2-}$ solid superacid is fabricated to enhance electrochemical performance of methanol (CH$_3$OH) catalytic oxidation. A novel honeycomb-like mesoporous SnO$_2$ is synthesized by the method of removing carbon sphere template. Sulfate ions are introduced into the SnO$_2$ to form the solid superacid SnO$_2$/SO$_4^{2-}$. Cheap nickel-based materials are dopped on the superacid to fabricate the NiO-SnO$_2$/SO$_4^{2-}$ materials. In the methanol catalytic oxidation，the NiO−SnO$_2$/SO$_4^{2-}$ catalyst exhibits the highest catalytic activity compared with NiO−SnO$_2$ and pure NiO. As a promoter, honeycomb-like SnO$_2$ with a larger surface and acid sites could offer more surface hydroxyl groups, which speeds the conversion of intermediate CO species to CO$_2$ so as to improve the electrocatalytic activity and poisoning-resistant of the catalysts. The present work provides a novel solid superacid nanomaterial and new opportunities to the rational design of catalysts with efficient catalytic performance for methanol.

1. INTRODUCTION

With the urgent demand for clean and portable energy, some new electrochemical devices such as high-efficiency fuel cells have attracted great attention[1]. Among various fuel cells, direct methanol fuel cells (DMFCs) which have the advantages of high methanol volumetric energy density, high energy conversion efficiency, low operating temperature, and low pollutant emissions, are considered to be ideal for meeting future energy needs[2, 3]. However, the reaction efficiency of DMFCs is confined due to some unresolved problems such as methanol crossover and sluggish methanol electro-oxidation kinetics[4]. Obviously, to find a suitable catalyst is one of the keys to enhance the methanol catalytic efficiency.

Ni based materials are considered as effective catalysts and have been widely used in energy conversion and storage reaction, such as methanol oxidation reaction (MOR), oxygen evolution reaction (OER), oxygen reduction reaction (ORR) and super capacitors[1, 5, 6]. Compared with previously developed precious metals, nickel-based materials are rich in resources, low cost and efficient surface oxidation performance, making it a promising alternative to precious metals[7-9]. However, due to poisonous intermediate CO species, which derives from the dissociation of CH_3OH and prevents the further oxidation of methanol, nickel-based materials have relatively poor catalytic efficiency in methanol oxidation. Therefore, a reasonable solution is to transform the poisonous intermediate CO into CO_2 faster through lots of surface hydroxyl groups (-OH) to improve its electrocatalytic activity and poisoning resistance[10].

Recently, metal oxides have attracted a great deal of attention as support materials owing to their excellent promoting effect. Among metal oxides, tin dioxide (SnO_2) as an n-type semiconductor is very stable and its lattice structure substrate allows for easy manipulation of pore size that make it a favorable support material[11]. The catalytic efficiency and stability of main catalyst can be improved by SnO_2 as a support[12, 13]. Therefore, SnO_2 is one of the most promising catalyst carrier materials in fuel cell due to its excellent chemical stability and the high promoting effect, especially under the anodic condition.

Sulfated solid superacid, distinguished from conventional liquid acids, has significant advantages of high catalytic-activity, rapid separation, easy recycling and low corrosivity[14]. Some metal oxides can be modified with sulfate ions to produce a high acidity, generally greater than that of 100 wt.% sulfuric acid and therefore becomes a solid superacid catalyst[15]. As an acidic catalyst, solid superacid presents Lewis acid sites through the induction of S=O group, and forms Brönsted acid sites through the ionization of water adsorbed on the Lewis acid sites, thus it can provide a large amount of surface hydroxyl group (-OH)[16].

According to the above, we designed and synthesized NiO loaded mesoporous SnO_2/SO_4^{2-} superacid materials as the catalyst for methanol oxidation. Here, NiO plays the role of main catalyst and the solid superacid, which has a larger surface and more surface hydroxyl groups, is the promoter of the catalyst. The honeycomb-like mesoporous solid superacid catalyst exhibits an enhanced electrocatalytic activity in comparison with pure NiO and NiO−SnO_2 catalysts for the methanol oxidation reaction, as well as the tolerance to CO poisoning.

2. EXPERIMENTAL

2.1 Materials

Glucose ($C_6H_{12}O_6$, Sinopharm Chemical Reagent) was used to prepare carbon spheres (CSs) templates. Nickel acetate tetrahydrate (NiAc, $Ni(CH_3COO)_2 \cdot 4H_2O$, Collins), tin tetrachloride pentahydrate ($SnCl_4 \cdot 5H_2O$, Maclean) and sulfuric acid (H_2SO_4, Sinopharm Chemical Reagent) were used for synthesizing the solid superacidcatalyst . Methanol (CH_3OH, Sinopharm Chemical Reagent) and Nafion solution (5.0 wt.%, Shanghai Yibang technology) were used in electrochemical testing.

Anhydrous ethanol (CH_3CH_2OH, Sinopharm Chemical Reagent) and deionized water were used as common lotions and solvents.

2.2 Synthesis of CSs

Carbon spheres were fabricated using glucose as carbon source via a traditional hydrothermal method with a few improvements. In brief, 6 g glucose was dissolved in 60 mL deionized water by stirring. Whereafter the solution was transferred into a Teflon-lined stainless-steel autoclave of 100 mL capacity and maintained at 180 ℃ for 8 h. After the reaction was completed, the autoclave was then allowed to cool naturally to room temperature. The black precipitates were filtered, washed with absolute alcohol and deionized water, and then dried at 60 ℃ for 12 h.

2.3 Synthesis of $NiO\text{-}SnO_2/SO_4^{2-}$

Briefly, the prepared carbon spheres were dispersed in 50 mL x mol/L $SnCl_4$ solution (x= 0.7, 1.0, 1.3, 1.6 and 1.9) under ultrasonication for 30 min. Subsequently the suspension was held at 40 ℃ for 8 h in water bath and the obtained products were collected by filtration. Then the white precipitates were calcined at 500 ℃ (heating rate of 1 ℃/min) for 2 h in air to remove the templates to obtain the honeycomb mesoporous SnO_2 (marked as S 1 to S 5). The obtained solid was ground and dispersed in 50 mL y mol/L NiAc solution (y=0.2, 0.4, 0.6, 0.8 and 1.0). Then the mixture was transferred into a autoclave of 100 mL capacity and maintained at 70 ℃ for 24 h. Subsequently, the sample was collected by filtration and calcined at 500 ℃ (heating rate of 2 ℃/min) for 3 h to generate the $NiO-SnO_2$. Afterwards, sulfuric acid solution (1 M) was added into the precursor with immersing for 1 h. The final product $NiO\text{-}SnO_2/SO_4^{2-}$ was obtained by calcination at 300 ℃, 400 ℃, 500 ℃ and 600 ℃ (heating rate of 2 ℃/min) for 4 h, respectively. As a comparison, the pure NiO were also synthesized by the method of calcining nickel salts. The complete synthesis process was sketched in Scheme 1.

2.4 Materials Characterization

X-ray diffractometer（XRD）spectrum was from a Bruker/D8 Adcance polycrystalline X-ray diffractometer. Scanning electron microscope (SEM) images were obtained on a FEI NovaNano SEM 450 microscope (USA). Transmission electron microscope (TEM) images were taken using a FEI Tecnai G2 F20 (USA). For TEM measurements, the samples were dispersed in ethanol and then dried on a holey carbon film Cu grid. Brunauer-Emmett-Teller (BET) isotherm measurements were conducted at 77 K using a Micromeritics TriStar II 3020 analyzer (USA). Fourier transform infrared (FTIR) spectrums were obtained using a Thermo Nicolet 380 FT-IR spectrometer (USA); X-ray photoelectron spectroscopy measurements were conducted using a Thermo ESCALAB 250XI multi-technical surface analysis system (USA). The IR spectra of absorbed pyridine (Py−IR) were also

obtained on a Nicolet 380 FT-IR spectrometer. The used thermogravimetric (TG) analyzer was TGA-50 (Japan).

2.5 Electrochemical measurements

The electrochemical measurements were carried out using CHI660E electrochemical workstation (Chenhua, Shanghai). Pt and Ag/AgCl were used as the counter and reference electrode, respectively. The working electrode was prepared by deposition of the catelysts on the surface of a glassy carbon electrode (GC). In simple terms, 2 mg of the catalyst, 8 µL Nafion solution and 400 µL of absolute ethanol were mixed and sonicated for several minutes. Subsequently, 10 µL mixture was deposited on the surface of the active area of the smooth GC electrode after well cleaning and polishing. The test electrolyte was a mixed solution with different proportions of methanol and sodium hydroxide. In order to ensure the optimization of experimental conditions, all electrochemical measurements were carried out with the scan rate of 100 mv^{-1} at 40 °C.
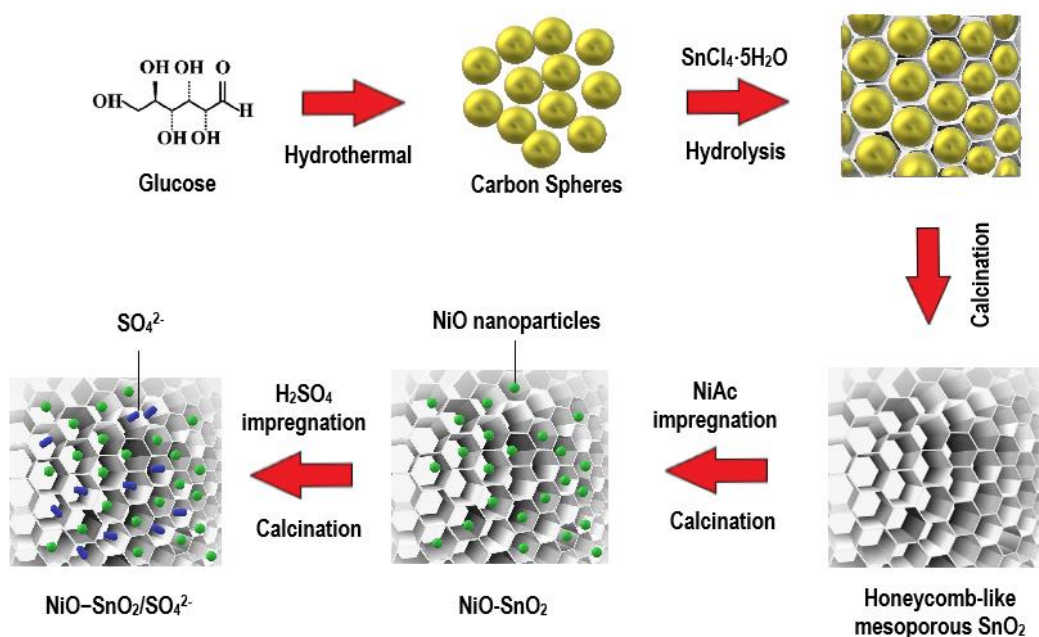
Scheme 1. Schematic illustration of the fabrication procedure of honeycomb-like mesoporous NiO−SnO$_2$/SO$_4^{2-}$.

3. RESULTS AND DISCUSSION

3.1 Microstructure study

3.1.1 SEM

The SEM image of the carbon spheres is displayed in Fig. 1a, showing a uniform diameter of about 100 nm. A series of honeycomb SnO$_2$ (S 1-S 5) synthesized with different concentrations of

Sn(IV) solution are shown in Fig. 1 (b-f). Fig. 1b shows the SEM image of S 1 that is synthesized with 0.7 M SnCl$_4$ solution and a porous structure resembling a honeycomb has formedpreliminarily, while the S 1 is not quite homogenous and regular.
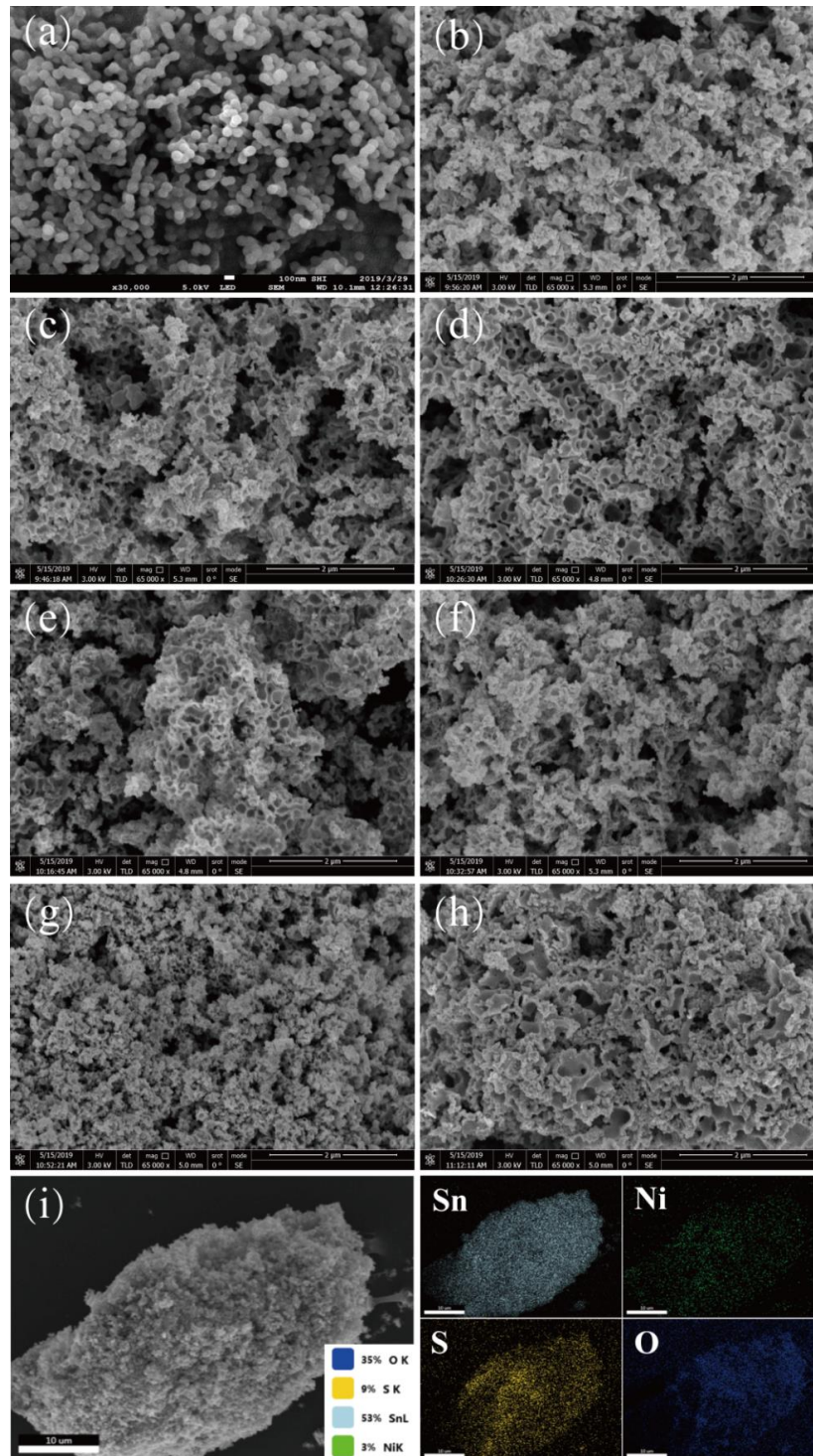

Figure 1. The SEM images of (a) carbon spheres, honeycombed SnO$_2$ synthesized with (b) 0.7 M, (c) 1.0 M, (d) 1.3 M, (e) 1.6 M, (f) 1.9 M Sn(IV) solution, (g) NiO−SnO$_2$ and (h) NiO−SnO$_2$/SO$_4^{2-}$ (i) the area scanning element mappings of NiO−SnO$_2$/SO$_4^{2-}$.

      With increasing of concentration of SnCl$_4$ solution, S 2 has a better honeycomb structure than that of S 1, as shown in Fig. 1c. Surprisingly, when 1.3 M solution of SnCl$_4$ is used, a well-defined honeycomb structure with the cell diameter between 100 - 200 nm can be obtained (Fig. 1d). Fig 1e and 1f show that the honeycomb structure gradually becomes less regular due to the rapid crystallization caused by higher concentration of SnCl$_4$. The SEM image of NiO−SnO$_2$ can be seen in Fig. 1g. The average diameter of the honeycomb decreases possibly due to the nickel oxide covering and the second calcination. The final sample NiO-SnO$_2$/SO$_4^{2-}$ is shown in Fig. 1h and it is clear that the honeycomb structure is damaged to some extent on account of the introduction of H$_2$SO$_4$. The EDS mappings are taken from the area in Fig. 1i, in which Sn, Ni, S, and O elements with uniform dispersion are detected, confirming that the NiO and SO$_4^{2-}$ are both distributed on the porous honeycomb SnO$_2$ homogeneously. The percentage of each element are 53%，3%，9% and 35%, respectively, as shown in the illustration.
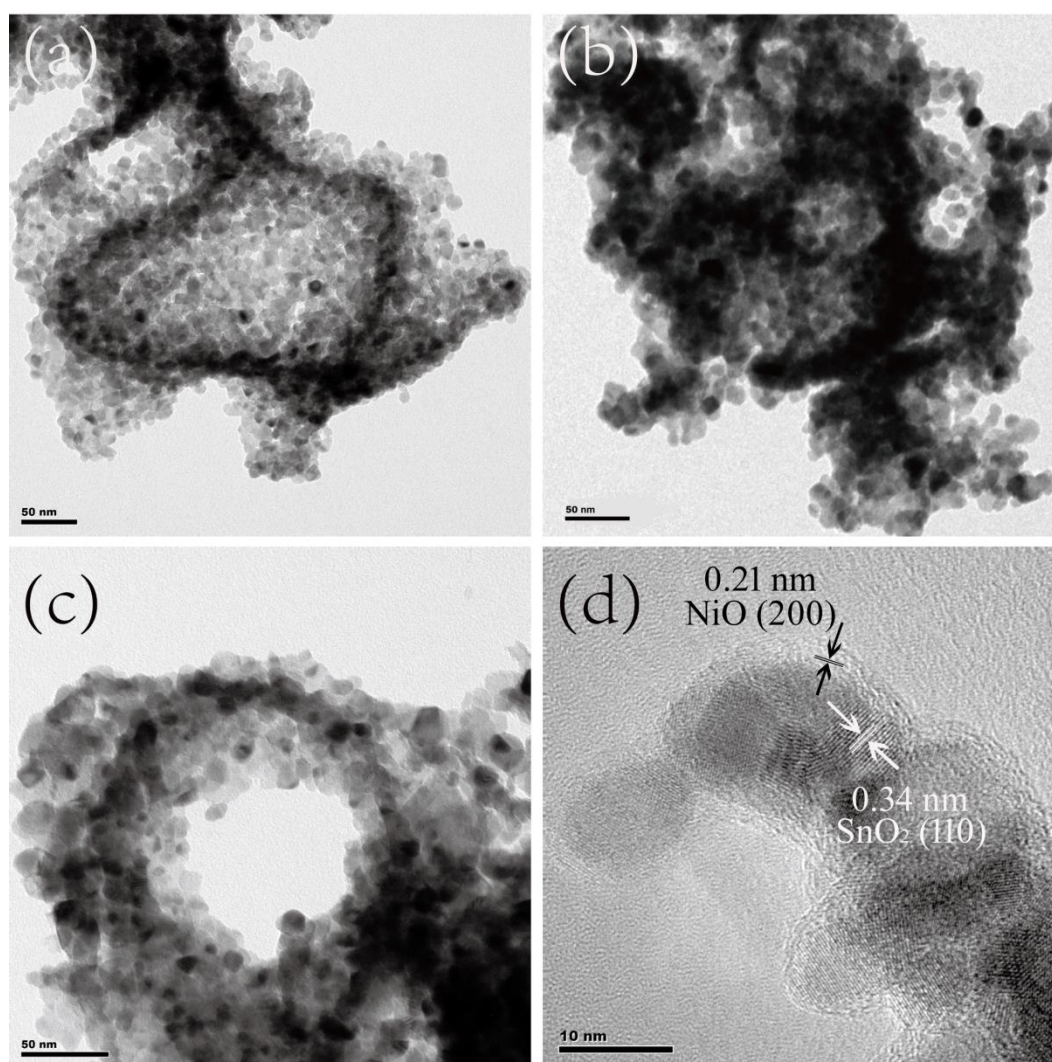
3.1.2 TEM

Figure 2. The TEM images of (a) SnO$_2$ (S 3), (b) NiO−SnO$_2$ and (c) NiO−SnO$_2$/SO$_4^{2-}$. (d) HRTEM image of NiO−SnO$_2$/SO$_4^{2-}$.

Fig. 2 displays the TEM images of pure SnO_2, NiO−SnO_2, NiO-SnO_2/SO_4^{2-}, respectively. A clear honeycomb cell with a diameter about 200 nm and the thick-ness of 20 nm which is composed of SnO_2 nanoparticles about 10-20 nm in diameter is shown in Fig. 2a. Fig. 2b shows the representative TEM image of the NiO−SnO_2 sample, in which the honeycomb structure with about 60 nm pore diameter is observed. The reduced pore size which is agreement with the result of SEM is caused by introduction of NiO and second calcination. The TEM image of NiO-SnO_2/SO_4^{2-} is shown in Fig. 2c and it exhibits that the structure is partly destroyed due to the addition of H_2SO_4, which can dissolve metallic oxide. Fig. 2d shows a typical HRTEM image of the NiO-SnO_2/SO_4^{2-}. Distinctly, a coating layer can be clearly seen on the surface of the SnO_2 nanoparticles, which proves the success of NiO modification. The measured lattice distances were 0.21 nm and 0.34 nm, corresponding to the (200) planes of NiO and (110) of SnO_2, respectively.

3.1.3 XRD

The crystal structure of honeycomb mesoporous NiO-SnO_2/SO_4^{2-} is confirmed by X−ray diffraction (XRD). Fig. 3 shows that the presence of diffraction peaks at 2θ = 26.6 °, 33.9 °, 37.9 °, 51.8 °, 54.8 °, 57.8 °, 61.9 °, 64.7 °, 65.9 °, 71.9 ° and 78.7 ° corresponding to the (110), (101), (200), (211), (220), (002), (310), (112), (301), (320) and (321) crystal planes, which can be indexed as the characteristic reflections of SnO_2 rutile phase (JCPDS. 41-1445). The weak peak at 2θ = 43.3°, corresponding to (200) crystal plane confirms the formation of NiO (JCPDS.47-1049). Moreover, the average crystallite size of SnO_2 is 17.9 nm calculated by the Scherrer Equation:

$$d = \frac{K\lambda}{\beta_{2\theta}\cos\theta}$$

where d is the average crystalline domain diameter in nm, K is the shape factor with a value close to 0.89, λ is the X-ray wavelength (Cu target 1.540 nm), $\beta_{2\theta}$ is the full width at half maximum (FWHM) in radians, and θ is the Bragg angle in radians. The calculation result is consistent with the crystallite size that can be seen in TEM images.
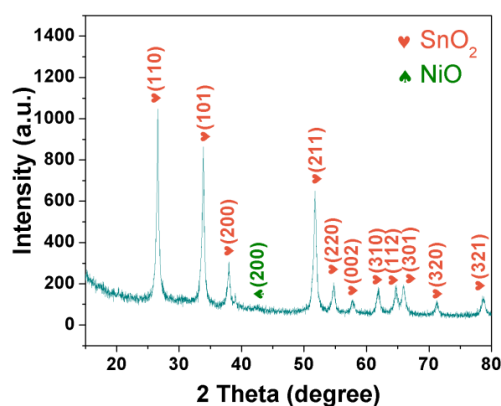

Figure 3. XRD pattern of the synthesized NiO−SnO_2/SO_4^{2-}.

3.1.4 XPS

In order to further characterize the surface composition，the XPS analysis of the NiO-SnO_2/SO_4^{2-} was conducted, as shown in Fig. 4. Fig. 4a shows the full-wide scanned spectrum indicating the presence of C, Sn, Ni, S and O in the sample. The Sn 3d spectrum of SnO_2 is shown in Fig. 4b, which displays a spin–orbit doublet centered at 487.2 eV and 495.6 eV corresponding to Sn $3d_{3/2}$ and Sn $3d_{5/2}$, respectively. The peak separation of 8.4 eV indicates a normal oxidation valence state of Sn^{4+} in the SnO_2 crystals[17, 18]. It can be seen that Ni 2p spectra of the sample can be fitted into six peaks in Fig. 4c and the peak at 856.2 eV is assigned to the Ni $2p_{3/2}$, while the peak at 873.8 eV is corresponding to Ni $2p_{1/2}$[19]. Fig. 4d displays the S 2p XPS spectrum. The peak corresponding to S 2p is obtained by fitting two components, one at about 169.0 eV and the other around 170.3 eV, both of which are sulfur oxidation states of +6[20]. Fig. 4e shows the O 1s spectra of the sample fitted into three peaks, and the binding energies at about 529.8 eV, 531.3 eV and 532.4 eV are correspond to the lattice oxygen (O_L), oxygen vacancies (O_V), and chemisorbed oxygen species (O_C) or OH species, respectively.[19] It's worth noting that the oxygen vacancy indicating the presence of unsaturation coordination of Sn which may be assigned to the Lewis acidic sites[21].
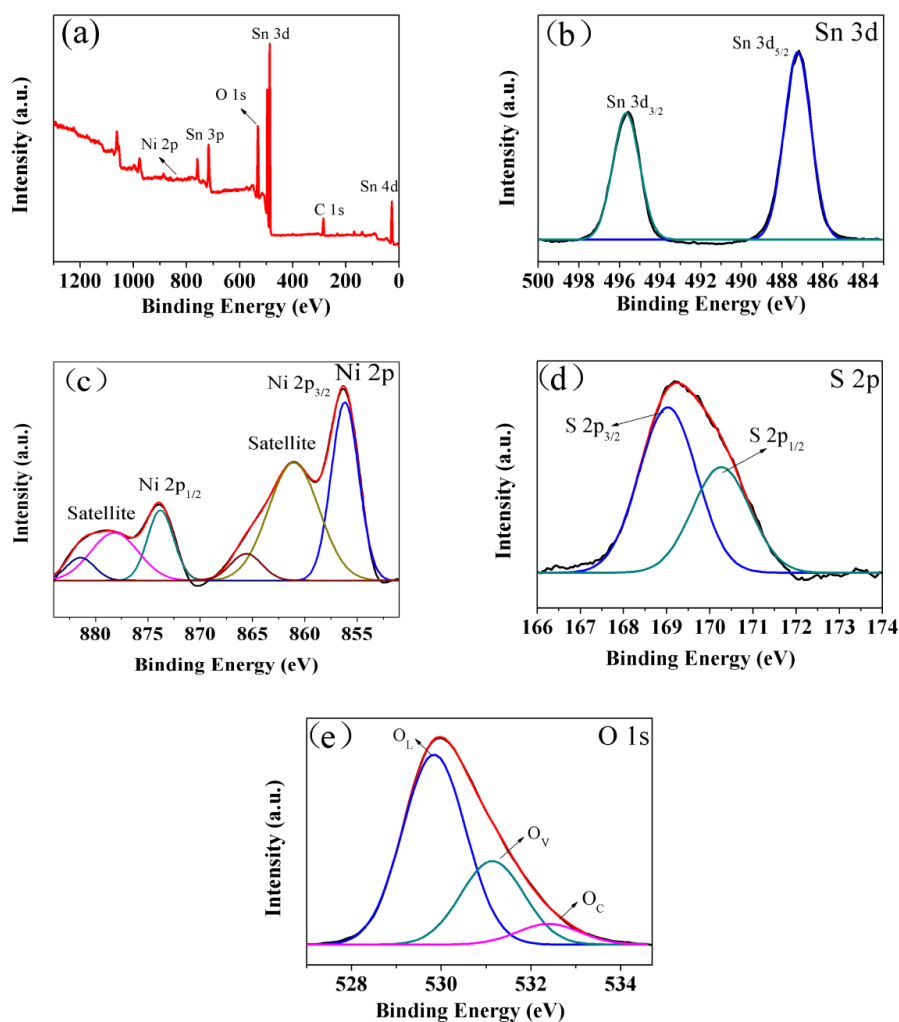

Figure 4. XPS spectrum of NiO−SnO_2/SO_4^{2-}: (a) full-wide scanned spectrum, (b) Sn 2p spectra, (c) Ni 2p spectra, (d) S 2p spectra and (e) O 1s spectra.

3.1.5 TG

The TG plot for the as-prepared $NiO\text{-}SnO_2/SO_4^{2-}$ along with the first derivative curve is shown in Fig. 5. As depicted in the figure, the three major regions for the loss in weight are translated as peaks in the first derivative curve. The first weight decrease (about 7.41 wt.%) corresponding to below 330 °C can be assigned to the loss of the physical water. The mass loss of 3.12 wt.% (about 330 °C ~ 700 °C) appears on the second stage in the figure corresponding to the desorption and decomposition of surface SO_4^{2-} groups on the catalyst surface[22]. Between 700 °C and 800 °C, the third stage of weight loss is approximately 3.94 wt.% due to the decomposition of the SO_4^{2-} thoroughly. This high temperature of decomposition suggests additional formation of bonds to Sn for the SO_4^{2-} species. Two terminals S-O are bonded to Sn in addition to coordination of a S=O group with Sn. These coordination sites of Sn are suggested to be the positions for water molecules to give rise to Brönsted acid sites[23].
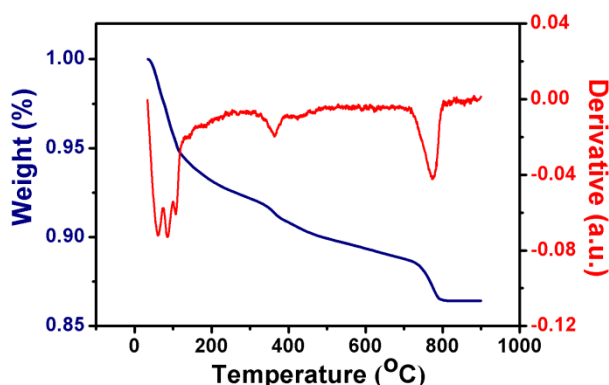

Figure 5. TG and DTG curves of $NiO-SnO_2/SO_4^{2-}$ obtained at 900 °C.
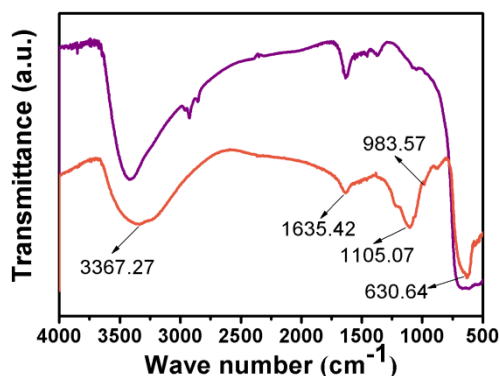
3.1.6 FT-IR

Figure 6. FT-IR spectra of $NiO-SnO_2$ and $NiO-SnO_2/SO_4^{2-}$.

The FT-IR spectra of $NiO-SnO_2$ and $NiO-SnO_2/SO_4^{2-}$ are displayed in Fig. 6. In both spectrums, the bands in the region around 630.64 cm^{-1} arise from Sn−O bridging stretches, and the

broad bands above 3000 cm^{-1} due to the stretching of hydroxyl groups (−OH bond)[24]. Compared with the NiO−SnO$_2$, the spectra of NiO−SnO$_2$/SO$_4^{2-}$ reveals the appearance of new bands characteristic of sulphate groups due to sulfation, with the strong peak at 1105.07 cm^{-1} assigned to S=O stretches of sulfated metal oxides and the peak at 983.57 cm^{-1} assigned to S−O stretches of sulfated metal oxides[25]. Thus the successful modification of sulfate ions on the NiO−SnO$_2$ particles is proved.

3.1.7 Py-IR

Fig. 7 shows the Py-IR spectra of the NiO-SnO$_2$/SO$_4^{2-}$ samples calcined at different temperatures during the introduction of sulfate ions after pyridine adsorption. The strong IR absorption bands around 1442 cm^{-1} and 1610 cm^{-1} are both assigned to adsorbed pyridine forming Lewis-type adducts. The produced peaks around 1539 cm^{-1} and 1635 cm^{-1} are taken the indication of pyridine interacting with Brönsted acid sites[26]. Moreover, the bands located at 1486 cm^{-1} corresponds to both of the Lewis acid sites and the Brönsted acid sites. Persuasively, as shown in Table 1, the amounts of acid sites in the four samples are clearly listed. The numbers of Brönsted acid and Lewis acid are 6.17 µmol/g，19.95 µmol/g in the sample calcined at 300 °C. The amounts of Brönsted acid and Lewis acid increase to 6.25 µmol/g and 22.59 µmol/g, respectively, when the calcining temperature is 400 °C, which may be caused by the different combination modes of sulfates and hydration degree[20]. When the temperature reaches 500 °C, the contents of Brönsted acid and Lewis acid both reach the maximum which are 33.73 µmol/g and 27.60 µmol/g. The result demonstrates that the best bonding degree between SO$_4^{2-}$ and SnO$_2$ is at 500 °C. However, the amounts of Brönsted acid, Lewis acid in the sample calcined at 600 °C are on the decline by reason of the decomposition of sulfate species on the surface.
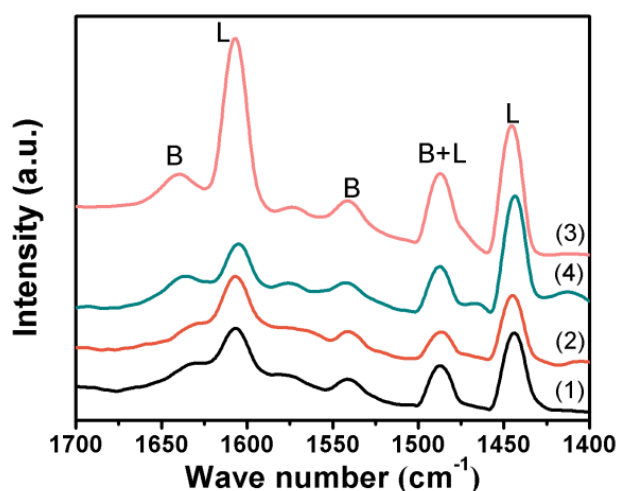

Figure 7. Py-IR spectra of NiO−SnO$_2$/SO$_4^{2-}$ calcined at (1) 300 °C; (2) 400 °C; (3) 500 °C; (4) 600 °C.

Table 1. The amounts of acid sites in NiO-SnO$_2$/SO$_4^{2-}$ calcined at different temperatures.

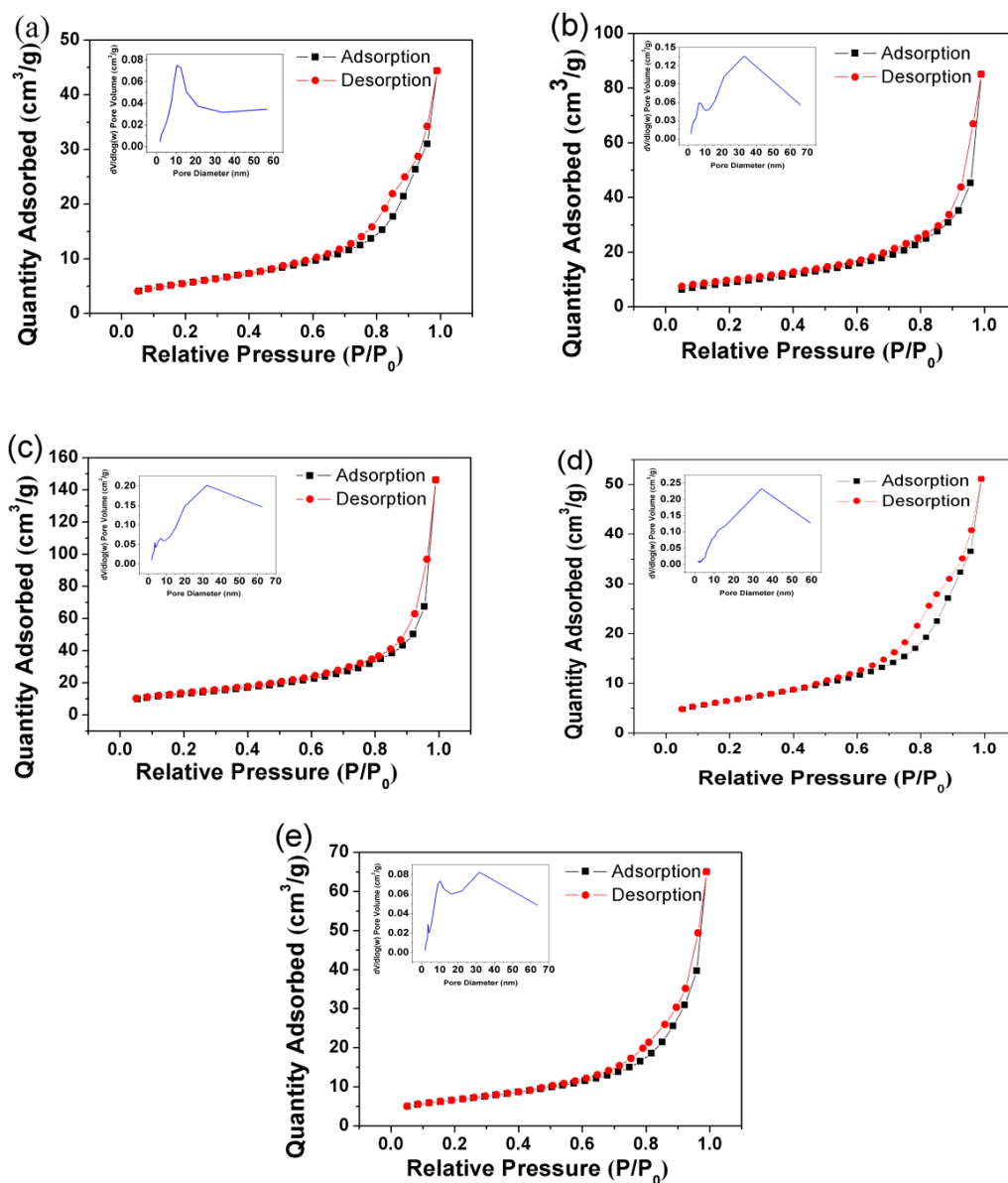| calcination temperature (°C)	Brönsted acid (μmol/g)	Lewis acid (μmol/g)	Total acid (μmol/g)
300	6.17	19.95	26.12
400	6.25	22.59	28.84
500	6.72	29.52	36.24
600	6.13	27.60	33.73

3.1.8 BET

Figure 8. Nitrogen adsorption-desorption measurement isotherm and the corresponding pore size distribution (inset) of honeycomb-like mesoporous SnO$_2$ (a) S 1, (b) S 2, (c) S 3, (d) S 4, (e) S 5.
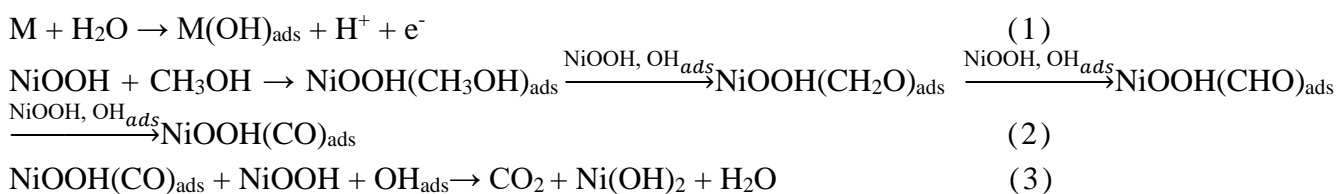
Nitrogen adsorption/desorption isotherms and corresponding pore size distributions of the honeycomb-like mesoporous SnO_2 (S 1-S 5) are shown in Fig. 8. All the materials exhibit type IV adsorption-desorption isotherms characteristic of mesoporous materials with a hysteresis loop. The physical properties of the samples including the specific pore diameter, pore volume and surface area are recorded in Table 2. The Brunauer-Emmett-Teller (BET) surface areas of the samples are found to be 19.90, 31.89, 46.51, 33.91 and 23.61 m^3g^{-1}, respectively. It is evident that S 3 has a larger specific surface area, which improves the adsorption and the transfer capacity for molecules[27]. The pore volume of S 3 is calculated to be about 0.23 cm^{-3}/g that is the largest, which indicates that it is beneficial to molecular diffusion and catalytic efficiency.

Table 2. The special surface area and pore size distribution of samples.

Sample	Specific surfacearea ($m^2 \cdot g^{-1}$)	Pore volume ($cm \cdot g^{-1}$)	Pore size (nm)
S 1	19.90	0.07	11.76
S 2	31.89	0.13	13.94
S 3	46.51	0.23	16.62
S 4	33.91	0.22	21.43
S 5	23.52	0.10	14.46

3.2. Electrochemical performance

The cyclic voltammetry (CV) curves of different catalysts under alkaline conditions are shown in Fig. 9. It can be seen that there is hardly current on GC and pure tin dioxide, namely no catalytic effect for methanol oxidation. The curve of pure NiO exhibits that there is catalytic effect on methanol with the oxidation peak current of 0.78 mA. As a comparison, the peak oxidation current (0.87 mA) of NiO−SnO₂ has been improved, because SnO_2 enhances the formation of Ni^{3+}/Ni^{2+} redox species and the formation of Ni^{3+} species is essential for alcohols oxidation process[28]. After sulfate ion modification, the peak current (1.0 mA) increases further. The onset potential and the oxidation peak potential of the two modified catalysts are similar, which are both at 0.35 V and 0.57 V. For the methanol oxidation atcatalysts modified electrodes in alkaline solution, the electrochemical catalytic reaction can be described as[29]:

$$M + H_2O \rightarrow M(OH)_{ads} + H^+ + e^- \qquad\qquad (1)$$

$$NiOOH + CH_3OH \rightarrow NiOOH(CH_3OH)_{ads} \xrightarrow{NiOOH,\ OH_{ads}} NiOOH(CH_2O)_{ads} \xrightarrow{NiOOH,\ OH_{ads}} NiOOH(CHO)_{ads}$$
$$\xrightarrow{NiOOH,\ OH_{ads}} NiOOH(CO)_{ads} \qquad\qquad (2)$$

$$NiOOH(CO)_{ads} + NiOOH + OH_{ads} \rightarrow CO_2 + Ni(OH)_2 + H_2O \qquad\qquad (3)$$

Electrocatalytic oxidation of methanol on the catalyst is carried out through the elementary steps of sorption of methanol and subsequent insertion of oxygen, leading to the formation of carbon dioxide. In the above reactions, the reaction 3, the oxidation of adsorbed CO is the rate determining process[30]. The mechanism of NiO-SnO₂/SO₄²⁻ superacid catalytic systems is shown in Fig. 11. The Brönsted acid sites are generated by the adsorbed of water on metal oxides neighboring sulfate group

with Lewis acid sites, which congest to more hydroxyl groups on the catalysts surfaces[31]. This facilitates the removal of partial oxidation intermediates from the surface through the faster converting from CO the CO_2, namely promoting the catalytic efficiency and preventing the poisoning of the surface[32].

Table 3 shows the comparison of the onset potential and current density with other catalysts. The onset potential is lower than that of other catalysts, which proves its excellent catalytic performance. The current density is not the greatest because the nickel content of the catalyst is only 3%.

Table 3. Comparison of the onset potential and peak current density between the $NiO\text{-}SnO_2/SO_4^{2-}$ in this work and other catalysts reported for methanol electrooxidation.

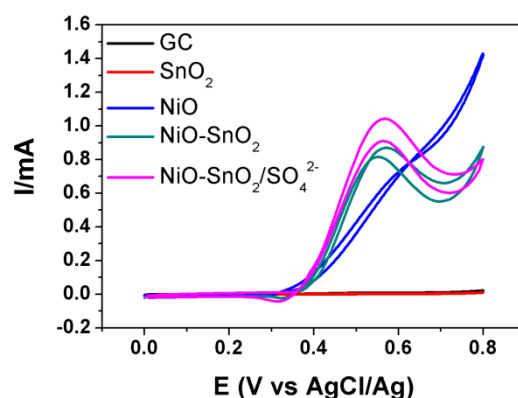| Catalysts	Scan rate (mVs^{-1})	Condition	Current density	Onset potential (V)	Ref.
$NiO\text{-}SnO_2/SO_4^{2-}$	100	1 M NaOH + 1M CH_3OH	12.2 mA cm^{-2}	0.32 (vs.Ag/AgCl)	This work
Ni-Co	50	0.1 M NaOH + 0.35 M CH_3OH	7.05 mA cm^{-2}	~0.42 (vs.SCE)	[33]
NiPO	50	0.5 M KOH + 0.5 M CH_3OH	44.97 mA cm^{-2}	0.65 (vs.Ag/AgCl)	[34]
NiO-Ni-P	50	0.5 M KOH + 1 M CH_3OH	28.56 mA cm^{-2}	0.32 (vs.SCE)	[35]
Ni_2Cu_1	50	1 M NaOH + 0.5 M CH_3OH	13.8 mA cm^{-2}	0.44 (vs.SCE)	[36]

Figure 9. CVs of different electrodes in 1.0 M NaOH and 1.0 M CH_3OH.
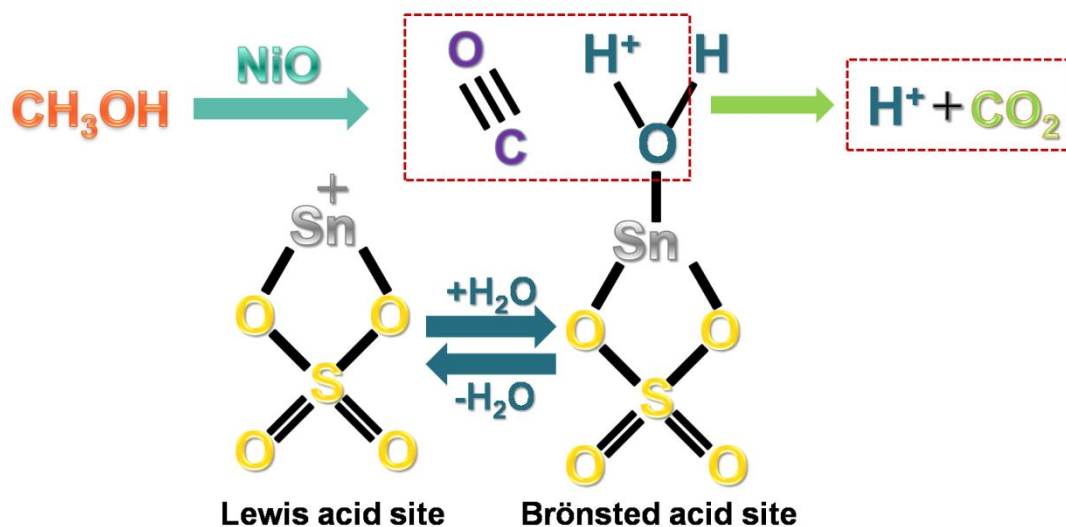
Scheme 2. Schematic illustration for the structure of Lewis and Brönsted acid sites and the removal of CO in the methanol catalytic oxidation process.

As shown in Fig 10, 100 voltammetry cycles are performed. It can be seen that the onset potentials, peak voltages are unchanged, meanwhie, the current decreases gradually in the first 70 laps. Subsequently, the peak current remains unchanged at about 1.1 mA after 70 laps, which demonstrates the good stability of NiO-SnO$_2$/SO$_4^{2-}$. In the continuous scanning process, two crystal phases of nickel electrode can be observed in each cycle. The first peak at 0.37 V and the second peak at 0.56 V are related to the α-Ni(OH)$_2$/NiOOH and β-Ni(OH)$_2$/NiOOH conversions, respectively. α-Ni(OH)$_2$, which is unstable in a strong base environment eventually ages to β-Ni(OH)$_2$[37]. As a mater of fact, β-NiOOH is perceived as the major active substance, which makes the cycles more stable and efficient the catalytic oxidation of methanol.
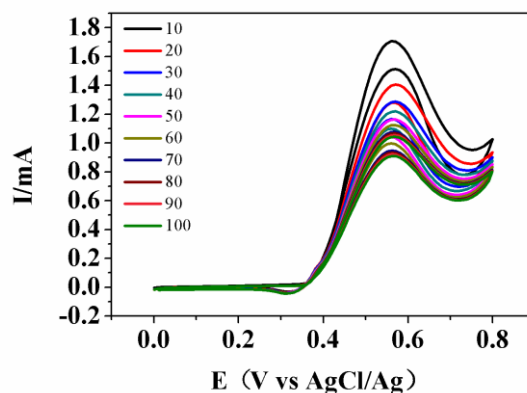

Figure 10. CVs of NiO−SnO$_2$/SO$_4^{2-}$ catalyst with different scanning cycles in 1.5 M NaOH and 1.5 M CH$_3$OH.

Fig. 11 shows the electrochemical performance of NiO-SnO$_2$/SO$_4^{2-}$ calcined at four different temperatures during the introduction of sulfate. As the calcination temperature increases from 300 to 600 °C, the peak current gradually increases and reaches the maximum at 500 °C, while the peak

current then decreases at 600 °C. Obviously, the result which is consistent with the result of Py-IR illustrates the efficiency of the catalyst depends on its acid amount. Moreover, the onset potential of the specimen calcined at 500 °C is the lowest among all the samples. Hence, the electrochemical performance results show that the catalytic oxidation of methanol is the best after 500 °C calcining.
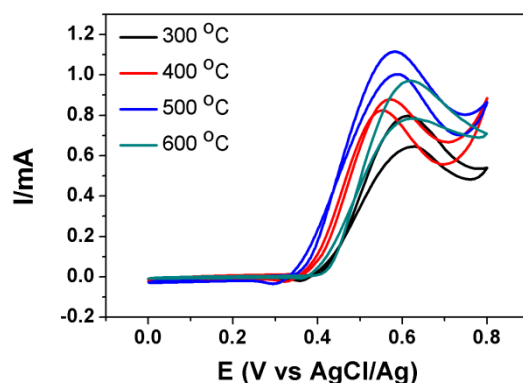

Figure11. CVs of NiO−SnO$_2$/SO$_4^{2-}$ catalyst calcined at different calcination temperatures.

The influence of nickel content on its electrochemical properties is shown in Fig. 12. As the main catalyst, the content of nickel affects the catalytic efficiency of methanol directly. As is shown, when the nickel content is 1 wt.%, the peak current is only about 0.5 mA. When the nickel content gradually increases, the peak current of methanol oxidation increases gradually and reaches the maximum (1.04 mA) at 3 wt.% of Ni content that is about twice as much as that of 1 wt. % content. Nevertheless, the catalytic efficiency decreases gradually when the content exceeds 3 wt.%, maybe due to the poisonous effect of CO produced in the oxidation process.
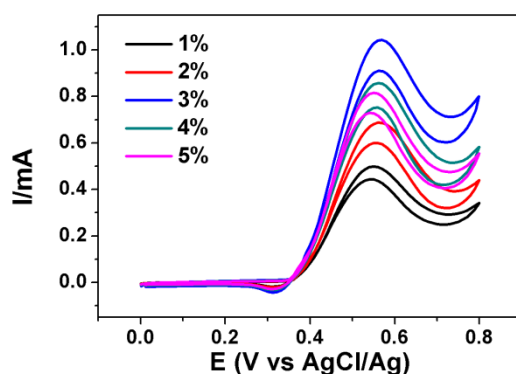

Figure12. CVs of NiO−SnO$_2$/SO$_4^{2-}$ catalyst with different nickel contents in 1.5 M NaOH and 1.5 M CH$_3$OH.

As shown in Fig. 13, study on the influence of methanol concentrationon catalytic oxidation efficiency is carried out. Methanol concentration is adjusted successively. From the cyclic voltammograms, it is clear that all curves show the oxidation peaks of methanol with an peak potential around 0.58 V. When methanol concentration is at 1.5 M, the highest methanol oxidation peak

occurred. According to the above reaction mechanism, the increase of methanol molecules can promote the forward the reaction, while the intermediate CO species produced by excessive methanol may cover the active sites to accelerate catalyst poisoning, which is corresponds to the decrease of peak current over the concentration of methanol at 1.5 M.
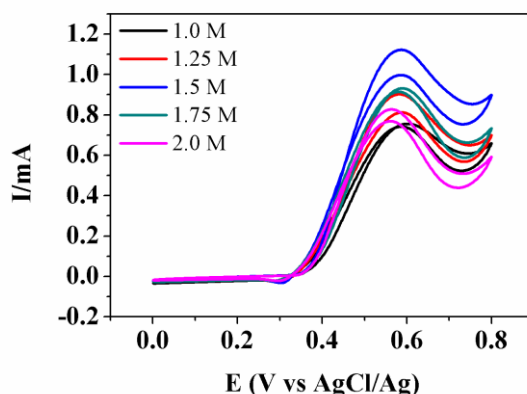

Figure 13. CVs of NiO−SnO$_2$/SO$_4^{2-}$ in 1.5 M NaOH and different concentrations of CH$_3$OH solution.

Fig. 14 showed the CVs of NiO-SnO$_2$/SO$_4^{2-}$ catalyst for methanol oxidation in different concentrations of NaOH solution. With the increasing of NaOH concentration in range of 1-2 M, the oxidation peak current gradually is improved, which is related to the adsorption of the –OH groups on the electrode, boosting the process of electron transfer, expediting the conversion of Ni^{3+}/Ni^{2+} and reaction rate[38]. The peak current reached the maximum （1.1 mA） at 1.5 M of NaOH solution. Adversely, when the concentration of NaOH increases to 1.75 M and 2 M, the current decreases to 1.02 mA and 0.85 mA, respectively, which is due to the competitive adsorption of CH$_3$OH and –OH.
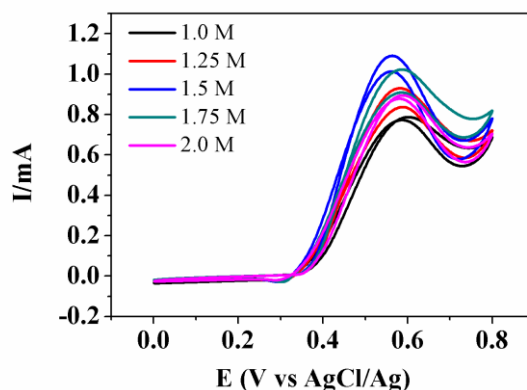

Figure 14. CVs of NiO−SnO$_2$/SO$_4^{2-}$ catalyst in 1.5 M CH$_3$OH and differentconcentrations of NaOH solution.

Stability testing is essential for catalysts. As shown in Fig 15, the current trends of different catalysts in continuous 10000 s under 0.6 V are studied. Apparently, the final current on pure NiO nanoparticles is only about 0.2 mA, while the final current on NiO-SnO$_2$/SO$_4^{2-}$ can be four times

higher. The rapid decay in the initial stage of both samples may be due to the double-layer discharge. Then, the current of NiO-SnO$_2$/SO$_4^{2-}$ tends to be relatively stable, but the current of pure NiO without the superacid has been decreasing. In short, superacid supported catalysts have better catalytic activity, toxicity resistance and stability.
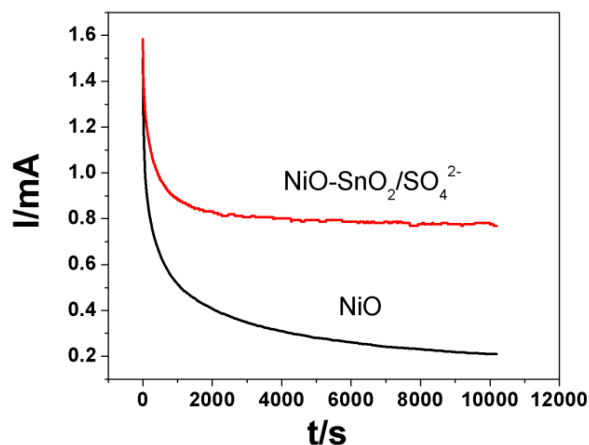

Figure 15. Time current curve of NiO−SnO$_2$/SO$_4^{2-}$ catalyst and pure NiO in 1.5 M NaOH and 1.5 M CH$_3$OH.

4. CONCLUSION

In summary, the honeycomb-like mesoporous SnO$_2$ is successfully synthesized through a well-designed sacrificial templating method. Afterwards, NiO and SO$_4^{2-}$ are modified onto the SnO$_2$ carrier to obtain a solid superacid. Here, nickel oxide is the main catalyst for methanol oxidation, honeycomb-like SnO$_2$/SO$_4^{2-}$ is a promoter providing more surface hydroxide ions and accelerating the transformation of intermediate CO species to CO$_2$. Compared with NiO, NiO-SnO$_2$/SO$_4^{2-}$ has a better poisoning resistance, stability and higher catalytic activity which is four times as that of NiO. NiO-SnO$_2$/SO$_4^{2-}$ is proved to be a suitable candidate for DMFC.

References

1. B. Dong, W. Li, X. Huang, Z. Ali, T. Zhang, Z. Yang, Y. Hou, *Nano Energy*, 55 (2019) 37.
2. J.H. Montoya, L.C. Seitz, P. Chakthranont, A. Vojvodic, T.F. Jaramillo, J.K. Nørskov, *Nat. Mater.*, 16 (2016) 70.
3. E. Sairanen, M.C. Figueiredo, R. Karinen, A. Santasalo-Aarnio, H. Jiang, J. Sainio, T. Kallio, J. Lehtonen, *Appl. Catal., B*, 148-149 (2014) 11.
4. P. Li, Y. Gu, Z. Yu, P. Gao, Y. An, J. Li, *Electrochim. Acta*, 297 (2019) 864.

5.   L.S. Yuan, Y.X. Zheng, M.L. Jia, S.J. Zhang, X.L. Wang, C. Peng, *Electrochim. Acta*, 154 (2015) 54.
6.   Y. Yu, Q. Yang, X. Li, M. Guo, J. Hu, *Green Chem.*, 18 (2016) 2827.
7.   P. Wang, Y. Zhou, M. Hu, J. Chen, *Appl. Surf. Sci.*, 392 (2017) 562.
8.   J. Li, Z. Luo, Z. Yong, J. Liu, T. Zhang, P. Tang, J. Arbiol, J. Llorca, A. Cabot, *Appl. Catal., B*, 234 (2018) 10.
9.   A.R. Jadhav, H.A. Bandal, A.A. Chaugule, H. Kim, *Electrochim. Acta*, 240 (2017) 277.
10. M.B. Askari, M. Seifi, S.M. Rozati, A. Beheshti-Marnani, M.H.R. Zadeh, *Chem. Phys. Lett.*, 706 (2018) 164.
11. Z. Merati, J.B. Parsa, *Appl. Surf. Sci.*, 435 (2017) 535.
12. M. Dou, H. Ming, L. Dong, W. Lu, Z. Shao, B. Yi, *Electrochim. Acta*, 92 (2013) 468.
13. F. Yang, J. Liu, H. Lu, H. Ping, D. Xu, *Electrochim. Acta*, 76 (2012) 475.
14. W. Yang, Y.S. Ok, X. Dou, Y. Zhang, M. Yang, D. Wei, P. Xu, *Environ. Res.*, 175 (2019) 393.
15. F.H. Alhassan, U. Rashid, M.S. Al-Qubaisi, A. Rasedee, T.Y. Yun, *Powder Technol.*, 253 (2014) 809.
16. J. Gardy, A. Osatiashtiani, O. Céspedes, A. Hassanpour, X. Lai, A.F. Lee, K. Wilson, M. Rehan, *Appl. Catal., B*, 234 (2018) 268.
17. S. Bai, J. Liu, J. Guo, R. Luo, D. Li, Y. Song, C.C. Liu, A. Chen, *Sens. Actuators, B*, 249 (2017) 22.
18. S. Bai, C. Liu, R. Luo, A. Chen, *Appl. Surf. Sci.*, 437 (2017) 304.
19. S. Zhang, Y. Li, G. Sun, B. Zhang, Y. Wang, J. Cao, Z. Zhang, *Sens. Actuators, B*, 288 (2019) 373.
20. H. Wang, Y. Li, F. Yu, Q. Wang, B. Xing, D. Li, R. Li, *Chem. Eng. J.,* 364 (2019) 111.
21. W. Xu, C. Chao, Y. Du, X.Z. Liu, X. Li, X. Xie, *Mater. Chem. Phys.*, 211 (2018) 72.
22. J. Fang, Z. Zheng, Z. Xu, S. Zheng, Z. Guo, L. Chen, *J. Hazard. Mater.*,134 (2006) 94.
23. M. Hino, M. Kurashige, H. Matsuhashi, K. Arata, *Thermochim. Acta*, 441 (2006) 35.
24. L. Wu, Y. Zhou, W. Nie, L. Song, P. Chen, *Appl. Surf. Sci.*, 351 (2015) 320.
25. J.L. Ropero-Vega, A. Aldana-Pérez, R. Gómez, M.E. Niño-Gómez, *Appl. Catal., A*, 379 (2010) 24.
26. C.A. Emeis, *J. Catal,* 141 (1993) 347.
27. A.M. Al-Enizi, M. Naushad, A.A.H. Al-Muhtaseb, Rukshana, S.M. Alshehri, Z.A. Alothman, T. Ahamad, *Chem. Eng. J.*, 345 (2018) 58.
28. H.B. Hassan, R.H. Tammam, Solid State Ionics, 320 (2018) 325.
29. R.M.A. Hameed, *Appl. Surf. Sci.*, 357 (2015) 417.
30. M.A. Abdel Rahim, R.M. Abdel Hameed, M.W. Khalil, *J. Power Sources*, 134 (2004) 160.
31. L. Li, H. Yue, T. Ji, W. Li, X. Zhao, L. Wang, J. She, X. Gu, X. Li, *Appl. Catal., A*, 574 (2019) 25.
32. Z. Na, Z. Sheng, C. Du, Z. Wang, Y. Shao, F. Kong, Y. Lin, G. Yin, *Electrochim. Acta*, 117 (2014) 413.
33. W. Wang, R. Li, X. Hua, R. Zhang, *Electrochim. Acta*, 163 (2015) 48.
34. X. Song, Q. Sun, L. Gao, W. Chen, Y. Wu, Y. Li, L. Mao, J.-H. Yang, *Int. J. Hydrogen Energy*, 43 (2018) 12091.
35. Y.Y. Tong, C.D. Gu, J.L. Zhang, H. Tang, X.L. Wang, J.P. Tu, *Int. J. Hydrogen Energy*, 41 (2016) 6342.
36. S. Samanta, K. Bhunia, D. Pradhan, B. Satpati, R. Srivastava, *Mater. Today Energy*, 8 (2018) 45.
37. S.N. Azizi, S. Ghasemi, N.S. Gilani, *Chin. J. Catal.*, 35 (2014) 383.
38. H. Cheshideh, F. Nasirpouri, *J. Electroanal. Chem.*, 797 (2017) 121.